COBEM 2021 26th International Congress of Mechanical Engineering
November 22-26, 2021, Virtual Congress, Brazil

COB-2021-1928
INFLUENCE OF HIGH INFLOW TURBULENCE ON THE AIRFOIL BOUNDARY LAYER AND WALL PRESSURE SPECTRUM

Jose Rendón-Arredondo
Alejandro Marulanda-Tobón
Universidad EAFIT. Medellin, Colombia
jmrendona@eafit.edu.co
amarula2@eafit.edu.co

Laura Botero-Bolívar
Leandro de Santana
University of Twente. Enschede, the Netherlands
l.boterobolivar@utwente.nl
leandro.desantana@utwente.nl

Abstract. *The main noise components produced by a single airfoil are the leading (LE) and trailing edge (TE). The former is caused by the interaction of the incoming turbulence with the airfoil leading, whereas the turbulence in the boundary layer produces the TE noise. In principle, the trailing edge noise is not affected by the inflow conditions. However, recent research demonstrated that high levels of inflow turbulence cause the free-stream turbulence to penetrate the boundary layer, changing the stationary and non-stationary parameters of the boundary layer. This study numerically analyzes the effect of the free-stream turbulence on the boundary layer thickness and mean velocity profile and its relation with the airfoil trailing edge noise. The far-field noise is predicted by low computational cost semi-empirical models with inputs provided by numerical simulations. Simulations considered a* $200mm$ *chord NACA 0012 airfoil subjected to inflow velocity of* $30m/s$*, corresponding to a Reynolds number of* 400000*. Convergence analysis and the extrapolation of Richardson were conducted to determine the independence of the grid refinement on the results. Numerical results were validated with experiments conducted at the Aeroacoustics Wind Tunnel facility of the University of Twente. The inlet turbulence intensity was varied from* 0% *up to* 30%*. Results showed a significant effect in the mean velocity profile and boundary layer thickness with a corresponding* $2-3dB$ *increase in the far-field noise for the entire frequency range.*

Keywords: *Trailing edge noise, Noise Prediction, High Inflow Turbulence, Boundary Layer, Richardson extrapolation*

1. INTRODUCTION

Worldwide concerns about reducing CO2 production have led to seeking new alternatives for the production of clean energy (Komninos, 2008). Harvesting the wind resources offered by urban environments is gaining force as a good alternative for the future environmentally-friendly cities. However, the exploitation of urban wind energy resources is still pending of societal and scientific breakthroughs.

Urban environments offer different work conditions in comparison to rural areas due to phenomena as flow acceleration, cannon effects, and pressure build-up caused by the different local geometries (Ricciardelli and Polimeno, 2006). The noise produced by horizontal and vertical axis wind turbines can be divided into mechanical and aerodynamic noise. Mechanical noise is generated by mechanical assemblies and can be significantly reduced by adequately dealing with the nacelle, whereas aerodynamic noise is caused by the interaction of the flow with aerodynamic surfaces, and therefore it is supposed to be observed at every operational condition (Deshmukh *et al.*, 2019).

he principal modern wind turbine noise sources are the leading edge (LE) and trailing edge (TE) (Oerlemans, 2011). The work of Deshmukh *et al.* (2019) demonstrates that the LE noise is caused by the turbulence present in the incoming flow, whereas the TE noise exists even with uniform inflow and is independent of inflow conditions up to a certain turbulence level. For this reason, TE noise is considered as self-noise.

TE noise is caused by the interaction of the turbulence in the turbulent boundary layer and the TE. The dangerous velocity components in the boundary layer generate pressure fluctuations in the airfoil surface close to the TE. The sudden change of impedance at the TE scatters such wall pressure fluctuations to the far-field as noise (Howe, 1978). Low levels of inflow turbulence do not affect the TE noise, which only depends on boundary layer parameters. However, previous researches by Dogan *et al.* (2016) have demonstrated that high levels of free-stream turbulence (FST) can penetrate the boundary layer and change its characteristics, which would affect the wall pressure fluctuations and consequently the TE

noise.

In this research, we aim at modeling the increment of the surface pressure spectra due to the high inflow turbulence. For that, low-cost stationary simulations were conducted in order to obtain the proper inputs for predicting the surface pressure spectra. The inflow turbulence level was varied from 0% to 30% each 10%. The length scale was held as constant at $0.06m$. The airfoil was a NACA 0012 of $200mm$ chord. Numerical simulations were validated by comparing the results with experiments conducted in the AeroAcoustics Wind Tunnel at the University of Twente under the same conditions (de Santana *et al.*, 2018).

The numerical simulation setup is explained, starting with the grid independence studies done. Then it shows the final mesh generated and relates it with the final computational domain and its boundary conditions. Later, the turbulence model is analyzed, and the numerical setup is validated using experimental data. Finally, the semi-empirical models used to calculate the surface pressure fluctuations are presented with their essential and interest variables.

The remain part of this paper is as follow: section 2. addresses the numerical simulations with the grid independence study, computational domain, models and results validation and the effect of the turbulence inside the boundary layer. Section 3. shows the prediction of the surface pressure fluctuations with a theoretical background and the sound level calculation.

2. NUMERICAL SIMULATION

Simulations were conducted in the commercial software Ansys 2019R3 using Fluent as the solver. Also, the most appropriated turbulence models to model the turbulent boundary layer were $Spalart - Allmaras$, $\kappa - \omega$ and $\kappa - \kappa_l - \omega$.

A NACA 0012 airfoil of $0.2m$ chord at 0° angle of attack was simulated with a constant inlet velocity of $30m/s$ and outlet relative pressure of $0Pa$. The maximum iteration number and length scale were kept constant at 500 and $0.06m$, respectively. The level of inflow turbulence was varied from 0.2% to 30%, with a delta of 10%.

2.1 Gird Independence

For reducing the simulation time without sacrificing precision in the results, a computational domain independence analysis and a grid independence were conducted in the following sections.

2.1.1 Computational domain independence

As a first approach and a convergence analysis of the size of the computational domain shown in Fig. 1 was conducted.

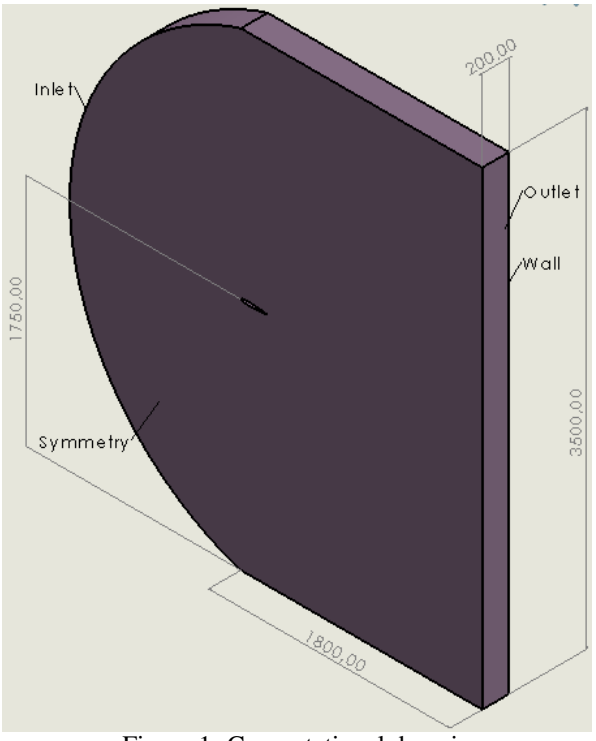

Figure 1: Computational domain

The computational domain independence analysis aims at reducing the distance d in Figure 1, varying its length from $1m$ and $2.4m$. To do this, the drag coefficient Cd was analyzed due to the $0°$ angle of attack and, in consequence, 0 value of the lift coefficient. A variation of less than 1% with respect to the previous value was sought, and the results are summarized in Tab. 1.

Table 1: Convergence analysis for $\kappa - \omega$ with d variation analyzing the drag force

d	# elements	DF (N)	Cd	% Cd
1	1.6×10^6	2.608	0.123	0.000
1.2	2.3×10^6	2.559	0.120	1.879
1.4	3.2×10^6	2.524	0.119	1.368
1.6	4.3×10^6	2.496	0.118	1.109
1.8	4.5×10^6	2.494	0.117	0.080
2	5.0×10^6	2.482	0.117	0.481
2.2	5.7×10^6	2.476	0.117	0.242
2.4	7.2×10^6	2.468	0.116	0.323

As can be inferred from Table 1 , the $\%Cd$ decreases when the element number and the d length increase, reaching the 1% variation when $d = 1.8m$. After that value of d, the change in the Cd variation is not significant. The computational domain was defined with a d of $1.8m$, which correspond to 9 times the airfoil chord.

2.1.2 Grid size independence

The element-size independence analysis was conducted adopting the Richardson extrapolation proposed by Roache (Roache, 1998). Such an extrapolation allows knowing what is the influence of the element size in the results obtained; comparing them with a hypothetical value of the mesh size would be zero.

Table 2 shows the five simulations made using different element sizes. The variable h refers to the characteristic length of the elements in each mesh, a variable that defines the scale of the physic system and is associated with an integration point. Finally, r refers to the refinement reason, calculated as $r = h_n/h_{n-1}$.

Table 2: Values used for the Richardson Extrapolation analysis extracted from Ansys.

Mesh Type	h	r	Elements	Drag Force (N)	Drag Coefficient
Ultra Fine	0.00438	NA	1.165.E+07	0.344	0.0162
Fine	0.00559	1.276	4.361.E+06	0.359	0.0169
Medium	0.00714	1.276	1.467.E+06	0.356	0.0168
Coarse	0.00908	1.271	5.575.E+05	0.372	0.0175
Ultra Coarse	0.0116	1.276	2.524.E+05	0.419	0.0197

Later, the expected value when the mesh size would be zero was calculated using Eq. (1), where p is a constant value proposed by Roache. To do so, the value of Cd for the fine and medium grid were selected and used as $f1$ and $f2$, respectively.

$$f_{exact} = f_1 - \frac{f_2 - f_1}{r^p - 1} \tag{1}$$

To confirm the correct implementation of the method, Roache proposed that the relative error (ϵ) between the value assumed as $f1$ and the exact value previously calculated is less than 2%. This error is calculated with the relationship in Eq. (2).

$$\epsilon = \frac{|f_{exact} - f_1|}{f_{exact}} \times 100 \tag{2}$$

After confirming that for this case, $\epsilon = 1.8\%$, the graph shown in Fig. 2 was made to analyze how far is the value obtained with the selected mesh in respect to the one where the element size can be taken as zero.

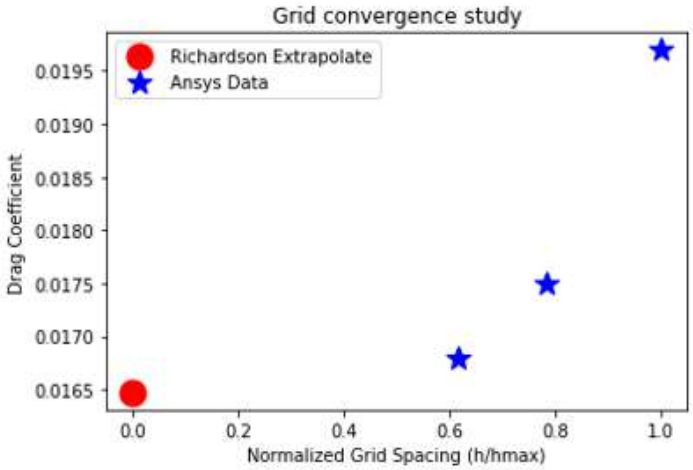

Figure 2: Grid convergence index (GCI)

Furthermore, the grid convergence index (GCI) calculates the tendency of the data to the value where the size of the grid is taken as zero. The GCI is calculated using Eq. (3), where F_s is a safety factor with a recommended value of 3.

$$GCI = \frac{= F_S|\epsilon|}{r^p - 1} \tag{3}$$

Roache proposed that the GCI value needs to be less than 5%, a condition that is achieved in this study where the value obtained is $GCI = 2.43\%$. Accordingly, with this analysis, the medium mesh refinement was used since it fits all the required values proposed by Roache.

Finally, when also the computational domain and the grid independence analysis were done, some mesh controls were applied to obtained a structured and refined mesh near the airfoil. The final mesh had $1.476E + 06$ elements with a mean value of *Element Quality = 0.73* and a *Skewness = 0.25* parameters that also helps to validate the developed grid shown in Fig. 3.

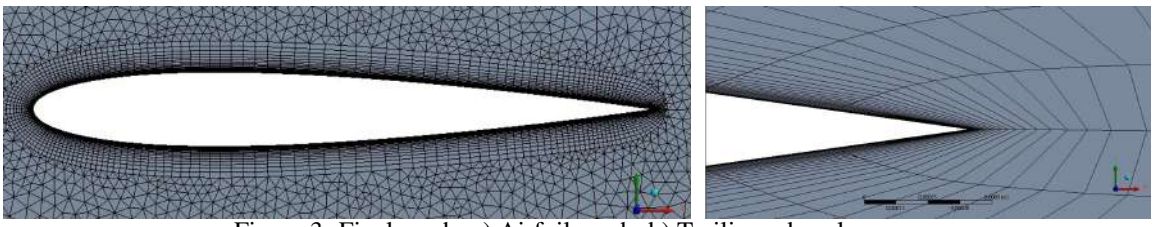

Figure 3: Final mesh. a) Airfoil mesh. b) Trailing edge close up.

2.2 Computational domain

In Figure 1, the computational domain was shown. Here, the inlet wall has a curve to reduce the total element quantity, the thickness of the domain is the same airfoil chord, and the parameter d is 9 times the airfoil chord, i.e., $d = 1.8m$.

For all the analysis, x is in the stream-wise direction while y is perpendicular to the airfoil chord and z s aligned with the airfoil span. This leads to define the inlet with a flow that is always in the x-direction. Also, the outlet was defined as a simple pressure outlet, a wall restriction on one side of the domain and a symmetry condition on the other side to simulate an infinite span for the airfoil. Figure 1 also shows the boundary conditions named before applied in the computational domain.

When the grid independence analysis was completed, the computational domain was also defined due to the length d and the element size of the mesh. This computational domain was shown in Figure 1 where as said $d = 1.8m$, the inlet wall has a curve to reduce the total element quantity, and asymmetry condition was applied to the side walls to represent an infinity airfoil.

2.3 Validation of turbulence model

To define the most suitable turbulence model, simulations at different inflow velocities were conducted, i.e., $\kappa-\kappa_l-\omega$, $\kappa-\omega$ and $Spalart-Allmaras$. In Fig. 4 the results obtained are shown.

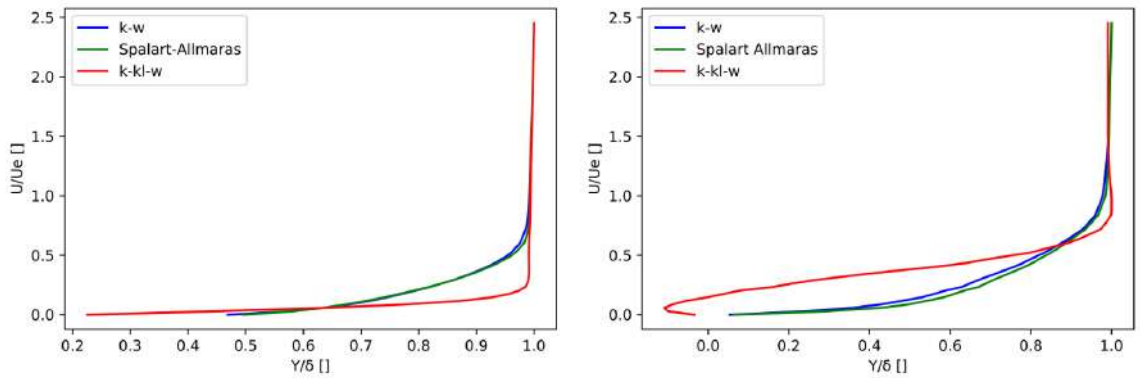

Figure 4: Turbulence model comparison. a) High Reynolds simulation ($30m/s$). b) Low Reynolds simulation ($10m/s$)

From Figure 4, it can be inferred that the model $\kappa-\kappa_l-\omega$ differs from the other models and present a non-expected behavior at $10m/s$. It can be concluded that the $\kappa-\kappa_l-\omega$ s not suitable for boundary layer modeling. Furthermore, there were no remarkable differences between the other two models. The $\kappa-\omega$ model was used since it incorporates two-equation and $Spalart-Allmaras$ only incorporates 1.

This model consists of a semi-empirical model that solves two transport equations, i.e., the first one solves the kinetic energy (κ) solving a factor associated with the turbulent kinetic energy. The second solve the turbulence dissipation rate (ω) which also depends on the kinetic energy factor and the dissipation rate (ϵ).

2.4 Validation of numerical setup

To validate the numerical results, comparisons with wind tunnel experiments were performed. For that, an additional simulation at $30m/s$ and 0% inflow turbulence was carried out (Botero-Bolívar *et al.*, 2021).

Comparisons consisted of the main velocity profile along the entire boundary and boundary layer thickness, i.e., the inputs needed for the semi-empirical models to calculate the surface pressure spectrum. To calculate the boundary layer thickness, two different approaches were adopted. The first approach calculates the boundary layer thickness as the location of the inflection point, which is the minimum value of the second derivative. This methodology reduces the influence of the noise inherent in the data (Küçükosman *et al.*, 2018). The second technique assumes the boundary layer thickness as the point in which the velocity reaches the value of 98.5% of the edge velocity. The calculated values for the experimental and simulated data are presented in Tab. 3.

Table 3: Data comparison of the boundary layer values.

Data	δ [mm]	U_e [m/s]
Experimental	5.21	25.61
Simulated	6.832	29.383
Error (%)	31.13	14.73

Figure 5 shows the mean velocity profile normalized by the external parameters, i.e., boundary layer thickness and edge velocity.

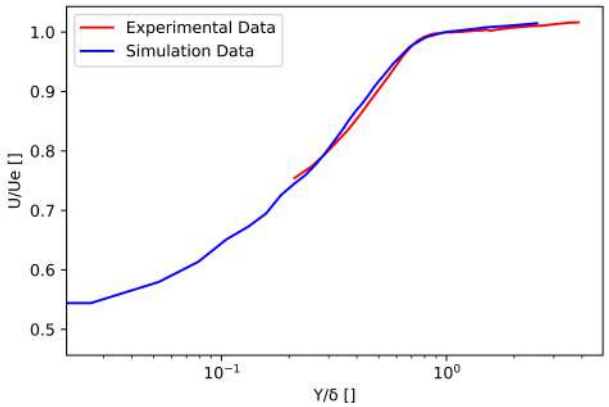

Figure 5: Normalized data comparison at $30m/s$ and $0\%Tu$.

In this graph, numerical and experimental results showed a good agreement, which validates the numerical methodology.

2.5 Effect of the turbulence in the boundary layer

As the first approach, the boundary layer profile was analyzed to verify if the inflow turbulence generates a change in the shape of the main velocity profile that could affect the surface pressure fluctuations. Figure 6 shows the mean velocity profile for the different levels of inflow turbulence.

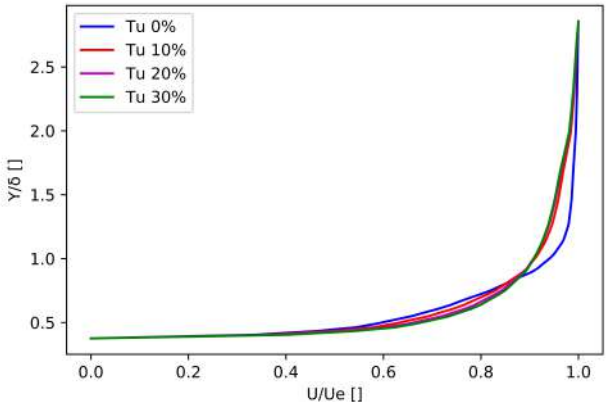

Figure 6: Normalized comparison for different turbulence levels

The boundary layer profile changes significantly when the turbulence level increases. There is a significant change in the velocity profile when the turbulence level is increased to 10%. However, there are no remarkable differences when the turbulence is increased from 10% to 30%. Furthermore, Tab 4 shows the boundary layer characteristics.

Table 4: Input variables for the model.

$\%TU$	τ_w[Pa]	U_e[m/s]	δ [mm]	δ^* [mm]	Θ [mm]	dP/dx
0	1.336	29.468	7.475	1.212	0.739	2954.024
10	1.49	29.216	11.515	1.296	0.87	2967.567
20	1.615	29.025	12.121	1.24	0.856	2994.85
30	1.683	28.911	12.323	1.199	0.838	3010.704

From Tab 4, it can be seen how the shear stress (τ_ω) generated in the wall and the pressure derivative increases when the turbulence level also increases. Also, the boundary layer thickness increases up to 55% on the case of 30% turbulence when compared with the case of uniform flow. This situation also causes a variation in the velocity of the boundary layer thickness and, in consequence, in the momentum and displacement thickness of the boundary layer. As this variable is used in the universal wall pressure spectrum equation, a variation in the PSD can be predicted.

3. PREDICTION OF SURFACE PRESSURE SPECTRUM

3.1 Theoretical background

To predict the surface pressure spectrum of each simulated case, transient simulations can be done, but also, semi-empirical models can be used. In this study, several semi-empirical models were implemented to predict the surface pressure spectra, using as input the steady simulations. Equation (4) shows the universal wall pressure model.

$$\Phi(\omega)SS = \frac{a(\omega FS)^b}{i[(\omega FS)^c + d]^e + [(fR_T^g)(\omega FS)]^h} \tag{4}$$

The parameters $a - i$ are specific to each semi-empirical model, the factor R_t includes the Reynolds number effect and SS and FS refer to the shape and frequency factor, respectively. Each of these factors also depends on each model. In this work, the wall pressure spectrum model proposed by Goody (Goody, 2004) and Kamruzzaman (Kamruzzaman *et al.*, 2015) was adopted. The models are presented in the following sections.

3.1.1 Goody

The model proposed by Goody (2004) was one of the first semi-empirical models applied. This model is known as the simplest or the baseline and is applied for simple, or zero pressure gradient flows. That is why the model was selected for this particular application. Table 5 presents the values of the model to be incorporated in equation 4.

Table 5: Parameters of the Goody model

a	b	c	d	e	f	g	h	i	m	FS	SS
3	2	0.75	0.5	3.7	1.1	-0.57	7	1	NA	δ/U_e	$U_e/\tau_w^2\delta$

3.1.2 Kamruzzaman

The model proposed by Kamruzzaman *et al.* (2015) model is derived from the model proposed by Rozenberg *et al.* (2012) for application where the flow has favorable and adverse pressure gradients. The model of Kamruzzaman was adopted in this work because it was proposed based on measurements of several types of NACA airfoils. The specific parameters for the Kamruzzaman model are shown in Tab 6.

Table 6: Parameters of the Kamruzzaman model

a	b	c	d	e	f
$0.45[1.75(\Pi_c^2\beta_c^2)^m + 15]$	2	1.637	0.27	2.47	$1.15^{-2/7}$
g	h	i	m	FS	SS
$-2/7$	7	1	$0.5(H/1.31)^{\cdot 3}$	δ^*/Ue	$Ue/\tau_w^2\delta^*$

The typical input parameters for the two models are boundary layer thickness (δ), velocity in the boundary layer thickness (U_e), shear stress in the wall (τ_ω), pressure derivative where the measurement is made (dP/dx), displacement thickness (δ^*) and momentum thickness (Θ). Such parameters are obtained from the post-processing of the simulation data.

3.2 Effect of the turbulence in the surface pressure fluctuations

Figure 7 shows the prediction of the wall pressure spectrum for different inflow turbulence levels.

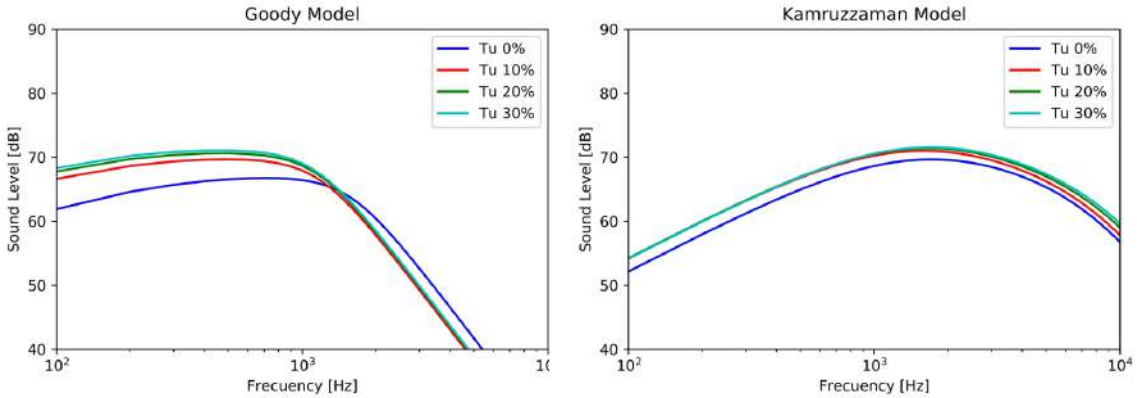

Figure 7: Semi-empirical models for different turbulence levels. a) Goody. b) Kamruzzaman.

For the Goody model can be seen that the sound level increases significantly, in $3dB$, in the low-frequency range up to a frequency of $1000Hz$ when the turbulence level goes from 0% up to 10%. For higher frequencies, the sound level decays rapidly for all cases and points to a similar value.

The Kamruzzaman model shows a parabolic behavior of the sound level, different from the obtained in the Goody model. Also, it differs in the value in low frequencies having a lesser value but sharing the peak with almost $70dB$ but in a higher frequency value, causing a lower decrease of the PSD.

Finally, in Tab. 7 the difference of the surface pressure is compared with the incoming turbulence level for each semi-empirical model used.

Table 7: Pressure average difference between the models.

$\%TU$	ΔdB [dB]	
	Goody	**Kamruzzaman**
0	0	0
10	3.198	1.118
20	2.921	1.847
30	2.797	2.211

4. CONCLUSION AND FUTURE WORKS

During the development of this work, several aspects can be highlighted. The first one is about the benefits and importance of developing a proper convergence and grid independence analysis; this leads to reduce in about 70% the number of elements used in the simulations and the time needed to solve the problem.

Also, the validation of the final numerical setup, including the turbulence model, by comparing the results with experiments help to increase the reliability of the simulations and all the process that are after this such as the surface pressure spectrum.

The correct choice of the semi-empirical models and the validation of the algorithm used to calculate the surface pressure fluctuations helps to increase the understanding of the phenomena.

With the values reported in Tab. 7, dependence between the surface pressure fluctuations and the incoming turbulence can be confirmed by obtaining a variation in each case, allowing a study of the dependency of these variables. Finally, it was confirmed that, as reported in the literature, the Kamruzzaman model represents in a better way this type of application. This due to the proportional increase of the dB variation with the turbulence percentage, a situation that does not happen with the Goody model.

Some future researches may be proposed due to the results obtained. The first one may be a close study of the relationship between the sound level variation and the turbulence level. However, the most important research we recommend focusing on is the development of a semi-empirical model that helps to predict with high reliability the surface pressure fluctuation for flows with high incoming turbulence.

5. REFERENCES

Botero-Bolívar, L., dos Santos, F.L., Venner, C.H. and de Santana, L.D., 2021. "The increase of the airfoil trailing edge noise and unsteady surface pressure due to high inflow turbulence". *AIAA Aviation and Aeronautics Forum and Exposition 2021*.

de Santana, L.D., Sanders, M.P., Venner, C.H. and Hoeijmakers, H.W., 2018. "The utwente aeroacoustic wind tunnel upgrade". In *2018 AIAA/CEAS Aeroacoustics Conference*. p. 3136.

Deshmukh, S., Bhattacharya, S., Jain, A. and Paul, A.R., 2019. "Wind turbine noise and its mitigation techniques: A review". *Energy Procedia*, Vol. 160, pp. 633–640.

Dogan, E., Hanson, R. and Ganapathisubramani, B., 2016. "Interactions of large-scale free-stream turbulence with turbulent boundary layers". *Journal of Fluid Mechanics*, pp. 1–29.

Goody, M., 2004. "Empirical spectral model of surface pressure fluctuations". *AIAA journal*, Vol. 42, No. 9, pp. 1788–1794.

Howe, M.S., 1978. "A review of the theory of trailing edge noise". *Journal of sound and vibration*, Vol. 61, No. 3, pp. 437–465.

Kamruzzaman, M., Bekiropoulos, D., Lutz, T., Würz, W. and Krämer, E., 2015. "A semi-empirical surface pressure spectrum model for airfoil trailing-edge noise prediction". *International Journal of Aeroacoustics*, Vol. 14, No. 5-6, pp. 833–882.

Komninos, N., 2008. "Intelligent cities". In *Electronic Government: Concepts, Methodologies, Tools, and Applications*, IGI Global, pp. 4205–4212.

Küçükosman, Y.C., Christophe, J. and Schram, C., 2018. "Trailing edge noise prediction based on wall pressure spectrum models for naca0012 airfoil". *Journal of Wind Engineering and Industrial Aerodynamics*, Vol. 175, pp. 305–316.

Oerlemans, S., 2011. "Wind turbine noise: primary noise sources".

Ricciardelli, F. and Polimeno, S., 2006. "Some characteristics of the wind flow in the lower urban boundary layer". *Journal of Wind Engineering and Industrial Aerodynamics*, Vol. 94, No. 11, pp. 815–832.

Roache, P.J., 1998. "Verification of codes and calculations". *AIAA journal*, Vol. 36, No. 5, pp. 696–702.

Rozenberg, Y., Robert, G. and Moreau, S., 2012. "Wall-pressure spectral model including the adverse pressure gradient effects". *AIAA journal*, Vol. 50, No. 10, pp. 2168–2179.

6. RESPONSIBILITY NOTICE

The authors are solely responsible for the printed material included in this paper.